Research Article

Direct laser-written aperiodic photonic volume elements for complex light shaping with high efficiency: inverse design and fabrication

Nicolas Barré[a,b,c] Ravi Shivaraman,[d] Simon Moser,[a] Patrick Salter,[d] Michael Schmidt,[b,c] Martin J. Booth,[c,d] and Alexander Jesacher[a,c,*]

[a]Medical University of Innsbruck, Institute of Biomedical Physics, Innsbruck, Austria
[b]Friedrich-Alexander-University Erlangen-Nürnberg, Institute of Photonic Technologies, Erlangen, Germany
[c]Friedrich-Alexander-University Erlangen-Nürnberg, Erlangen Graduate School in Advanced Optical Technologies, Erlangen, Germany
[d]University of Oxford, Department of Engineering Science, Oxford, United Kingdom

Abstract. Light plays a central role in many applications. The key to unlocking its versatility lies in shaping it into the most appropriate form for the task at hand. Specifically tailored refractive index modifications, directly manufactured inside glass using a short pulsed laser, enable an almost arbitrary control of the light flow. However, the stringent requirements for quantitative knowledge of these modifications, as well as for fabrication precision, have so far prevented the fabrication of light-efficient aperiodic photonic volume elements (APVEs). Here, we present a powerful approach to the design and manufacturing of light-efficient APVEs. We optimize application-specific three-dimensional arrangements of hundreds of thousands of microscopic voxels and manufacture them using femtosecond direct laser writing inside millimeter-sized glass volumes. We experimentally achieve unprecedented diffraction efficiencies up to 80%, which is enabled by precise voxel characterization and adaptive optics during fabrication. We demonstrate APVEs with various functionalities, including a spatial mode converter and combined intensity shaping and wavelength multiplexing. Our elements can be freely designed and are efficient, compact, and robust. Our approach is not limited to borosilicate glass but is potentially extendable to other substrates, including birefringent and nonlinear materials, giving a preview of even broader functionalities, including polarization modulation and dynamic elements.

Keywords: integrated photonics; holography; mode conversion; inverse design.

1 Introduction

Light has become an indispensable tool in our modern-day societies. It plays the central role in countless technological solutions, such as in the information transport along glass fibers or in various display, imaging, and sensing applications.[1] The increasing significance of light as a tool sparked a sharply rising demand for technologies that enable the temporal and spatial sculpting of light in user-defined ways.[2–4]

Of notable importance are so-called multiplexing applications, where one of many predefined output fields can be created upon presenting a unique predefined input field. Elements that can handle such tasks with high efficiency would find numerous applications in the analysis and synthesis of light fields. Examples range from conventional spectroscopy to complex tasks around information processing and transport. Mode-division multiplexing, for example, is a potential solution for avoiding the threat of reaching an upper limit in communication speed (capacity crunch).[5–8] Meanwhile, optical computing is currently experiencing a revival due to novel ways of manufacturing

*Address all correspondence to Alexander Jesacher, alexander.jesacher@i-med.ac.at

computer-designed optical networks that enable sophisticated data processing at the speed of light.[9–13]

Optically recorded volume holograms, e.g., from photorefractive materials,[14] have traditionally been used for multiplexing applications.[15,16] However, creating such holograms requires the realization of matching physical interference patterns at the recording step, and the approach is also limited to photosensitive substrates, which severely limits its practical applicability.

Aperiodic photonic volume elements (APVEs) can circumvent these limitations: they are designed on the computer and open to a multitude of different manufacturing techniques. For instance, they can be directly written into a substrate by locally changing its three-dimensional (3D) refractive index (RI) distribution in a voxel-by-voxel fashion. However, a major challenge in the production of APVEs is to meet the high accuracy requirements for manufacturing, since producing an efficient APVE puts high demands on the ability to modify the 3D RI distribution with high precision. Since the output light field arises from the interference of thousands of scattered waves, even small errors made on the voxel-scale quickly accumulate and severely degrade the output field quality. For this reason, past demonstrations of manufacturing APVEs in glass have been limited to proof-of-concept studies with rather low diffraction efficiencies[17] or restricted to two-dimensional (2D) configurations.[18] Recently, two-photon polymerization additive manufacturing of multilayer holograms[9] and the fabrication of 3D-graded index materials[10] have been demonstrated.

Here, we introduce an approach for realizing APVEs using direct laser writing in transparent dielectric media, such as glass. Our method allows for obtaining high diffraction efficiencies of up to 80%, many times more than what could previously be achieved.[17] This is made possible by employing precise tomographic voxel characterization[19] in combination with a design algorithm based on numerical beam propagation and the use of adaptive optics to ensure space-invariant voxel shapes throughout the full body of the APVE. We experimentally demonstrate the design and manufacture of three different, highly integrated APVEs that are optimized for intensity shaping, spatial mode, and wavelength multiplexing.

We believe that our results represent an important step toward the realization of robust and highly integrated 3D light shapers for many important application fields, such as information transport,[8] optical computing,[9–13] imaging through multimode fibers,[20] and nonlinear photonics.[21] They may further help to obtain fundamental insights in the behavior of quantum states of light upon scattering.[22]

2 APVE Concept

Figure 1(a) shows the basic concept of our photonic volume element, which is a laser-processed 3D region inside a glass substrate containing hundreds of thousands of spatially separated voxels of modified RI at predefined positions. Our approach is based on past demonstrations of direct laser-written aperiodic volume optics[17] but is also inspired by previous work on computer-generated 2D holograms based on waveguides.[23]

A single voxel measures only $1.75~\mu m \times 7.5~\mu m \times 10~\mu m$ and is created by moving the z stage (the long horizontal axis) for $10~\mu m$ during exposure to the laser focus. Fabrication of the whole device takes about 20 min. The quantitative RI profile of a single voxel across the $x - y$ axes, fabricated in Eagle glass, is shown in Fig. 1(b). This profile must be precisely known, as it serves as the basis for the numerical design process. The RI profile characterization is performed in a home-built tomographic microscope.[19] The RI distribution of each voxel is assumed to be invariant along the z direction. The input and output fields of the
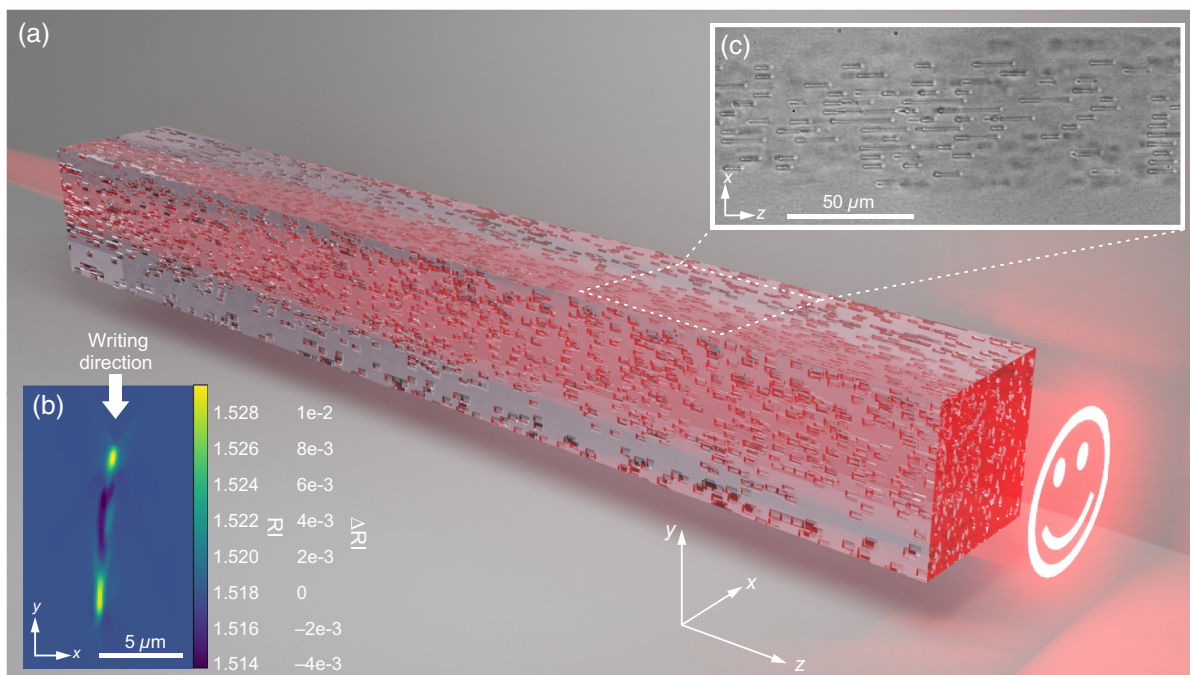

Fig. 1 Light manipulation with an APVE. (a) Sketch of a laser-processed glass substrate containing many voxels of modified RI. (b) Tomographically measured RI cross section of a single voxel. (c) Wide-field image taken from a fabricated device.

APVE are coupled through its smallest end facets. A wide-field transmission image of a fabricated APVE is shown in Fig. 1(c).

Our design algorithm operates on a Cartesian grid of size $I \times J \times K$, following the directions (x, y, z) of the coordinate system sketched in Fig. 1(a), which defines potential voxel positions. For our demonstrators, $I = 55$, $J = 14$, and $200 \leq K \leq 400$, depending on the device extension along the propagation direction z. This corresponds to a maximum number of voxels, varying between 154,000 and 308,000. The number of voxels in the transverse x and y directions is quite different due to the elongated nature of our reference voxel represented in Fig. 1(b). Basically, the algorithm simulates the light flow through the device using a beam propagation method[24] and decides upon the activation of a voxel, depending on whether it would improve the output wavefront or not. In our experimental demonstration, we explored only binary designs made of identical voxels depicted in Fig. 1(b), but the inverse design algorithm we implemented generalizes well to multilevel RI modifications. Details about this algorithm are provided in the Supplemental Material (Sec. S5).

The successful implementation of our APVE requires not only precise knowledge about the voxel properties but also the manufacturing abilities to produce the same profile reliably at all targeted substrate depths. This can be ensured using dynamic wavefront control, which compensates for spherical aberrations arising when focusing the laser into the substrate.[25] Further information about the manufacturing is provided in the Supplemental Material (Sec. S4).

3 Results

In the following sections, we explore three types of APVEs, designed for specific applications with different levels of complexity. The first one is a single-mode intensity shaper with a length of only 2 mm and is discussed in Sec. 3.1; the second one is a multicolor (RGB) multiplexer of 3 mm length and is discussed in Sec. 3.2. Finally, a Hermite–Gaussian (HG) six-mode sorter of 4 mm length is discussed in Sec. 3.3.

3.1 Sculpting Intensity Distributions

Our APVEs can be optimized to shape user-defined intensity patterns with high efficiency. To demonstrate this, we designed and fabricated an element producing a microscopic "smiley" at its output facet (i.e., the last layer of voxels) when read out with a Gaussian beam at a zero-degree readout angle (vacuum wavelength $\lambda_0 = 640$ nm, waist $w_0 = 40$ μm). The physical dimensions of the element are 0.1 mm $\times$ 0.1 mm $\times$ 2 mm, and

it contains $55 \times 14 \times 200$ voxels. As mentioned earlier, the unequal grid sizes along the x and y directions are due to the anisotropic voxel shape, which is a consequence of the same anisotropic shape of the focus creating the voxel. The device itself, i.e., the 3D region containing fabricated voxels, is embedded inside a larger glass chip for easier handling.

Figure 2 shows the results obtained with this APVE. It shows the designed output intensity template for a Gaussian input of 40 μm waist as well as the simulated and experimentally obtained results. The simulated result was obtained by numerical propagation of the input beam through a computer model of the optimized voxel arrangement. It thus marks an upper limit for the quality achievable in the experiment. The experimental result was obtained by imaging the output plane with a regular wide-field microscope (see Sec. S1 of the Supplemental Material for additional information about the experimental APVE characterization).

The diffraction efficiency of the APVE has been determined by calculating an overlap integral of the target amplitude pattern u_t with the simulated and experimentally measured output amplitude patterns u_{out} over the area of the observable end facet A,

$$\eta = \left| \int_A u_t u_{out}^* \mathrm{d}A \right|^2, \qquad (1)$$

where the powers of u_t and u_{out} are both normalized to 1. We introduce another efficiency metric η_{tot}, which further takes into account scattering losses into nonobservable angles,

$$\eta_{tot} = T\eta, \qquad (2)$$

with transmission factor $T \leq 1$. Therefore, η quantifies the power fraction of the measurable output light [the light arriving at the (simulated or real) camera plane], which is effectively turned into the target distribution, whereas η_{tot} is the respective conversion efficiency for the input beam. Losses due to Fresnel reflections at the input/output facets of the APVE are neglected in this consideration.

The theoretical and experimental diffraction efficiencies η_{tot} of the smiley converter are 90% and 80%, respectively. We note that $T \approx 1$ for the smiley shaper in both simulation and experiment, i.e., the number of scattering losses is close to zero. Since this application aims at intensity-only shaping, the phase distributions of u_t and u_{out} are irrelevant and thus assumed to be flat in Eq. (1). We further derived an error metric ϵ, defined as the root mean square difference between the normalized target
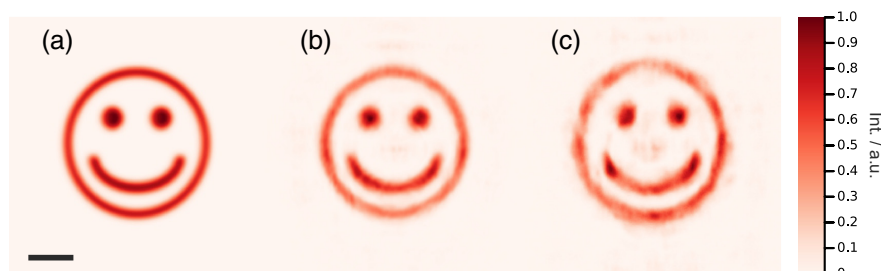

Fig. 2 Results from a smiley generator. (a) Designed output intensity; (b) simulated readout; (c) experimental result. The total light efficiency η_{tot} of the experimental result is about 80%. The scale bar measures 20 μm.
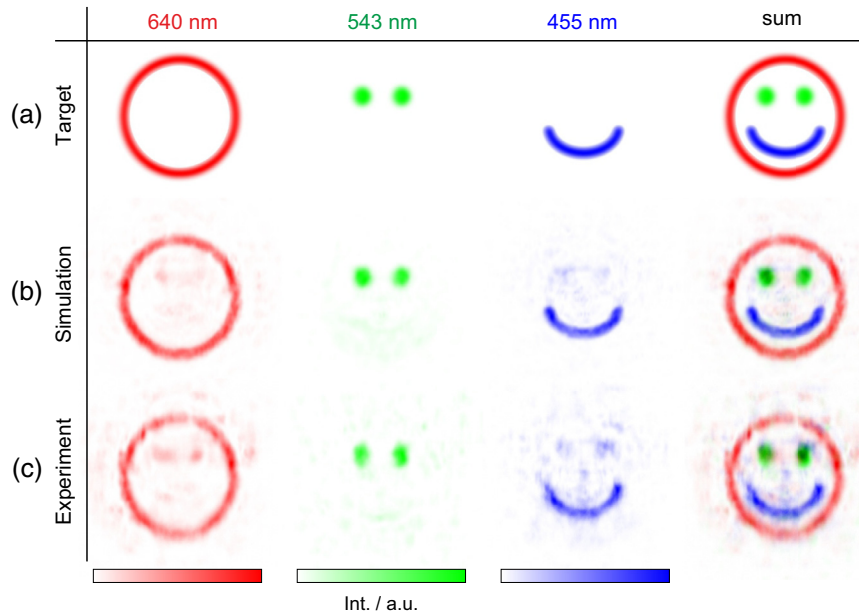
Fig. 3 Wavelength multiplexing. Different parts of the smiley appear, depending on the readout wavelength. (a) Target intensity patterns used for the APVE design. (b) Results from a simulated readout. (c) Experimental readouts.

and the simulated/experimental output intensities. We find $\epsilon_{\text{sim}} = 0.25$, and $\epsilon_{\text{exp}} = 0.35$.

Therefore, even though the intensity shaping shown here can be easily achieved using 2D diffractive optical elements, we are nevertheless able to simply demonstrate that our computational design approach can be faithfully implemented through the experimental characterization and reproducible manufacture of 3D voxel arrangements inside glass.

3.2 Wavelength Multiplexing

We demonstrate the feasibility of color multiplexing by designing and fabricating a multicolor smiley shaper, where different parts of the smiley (eyes, mouth, and head) appear only for specific readout wavelengths, as shown in Fig. 3. This APVE measures $0.1\text{ mm} \times 0.1\text{ mm} \times 3\text{ mm}$ and contains $55 \times 14 \times 300$ voxels. When read out at 640 nm with a beam waist of $w_0 = 40\ \mu\text{m}$, only the circular head appears at the output. Similarly, the eyes appear for a readout wavelength of 543 nm ($w_0 = 30\ \mu\text{m}$) and the mouth for 455 nm ($w_0 = 20\ \mu\text{m}$). Results obtained from simulated readouts and experiments using fiber-coupled lasers (see Sec. S2 of the Supplemental Material for details) are summarized in Fig. 3. The image table depicts false-color intensity distributions at the output facet of the APVE, which are individually normalized to their respective peak intensities. The fourth image column on the right shows a computer-generated overlap of the three readouts.

The simulated and experimentally determined power conversion efficiencies η from the three Gaussian input beams to the respective facial structures are summarized in Table 1. The table values are calculated using Eq. (1), i.e., they show which percentage of the output laser power is shaped into the respective facial structures. The average simulated efficiency over all colors is 67% for the simulation and 55% in the experiment. From the table values, it is noticeable that, in particular, the blue wavelength shows the largest disparity between simulation and

experiment, with an efficiency of 64% in the simulation and 49% in the experiment. This may be attributed to small remaining differences between the assumed and real voxel profiles at length scales of a few hundred nanometers. Such small irregularities will especially affect shorter wavelengths and are likely to be overlooked by our tomographic voxel characterization method, which employs the same wavelength for inspection and a smoothing total variation norm regularizer.[19] The simulated and experimentally measured transmission values T for all three readout wavelengths are shown in Table 2. We observe well-matching numbers between simulation and experiment for the red and green wavelengths, whereas the blue transmission value is around 25% lower in the experiment than predicted by the simulation.

Table 1 (a) Simulated and (b) experimentally obtained conversion efficiencies η. For each wavelength, the numbers state the respective percentage of the output power forming head, eyes, and mouth.

λ_0/nm	Head	Eyes	Mouth
(a)			
640	**77**	2	1
543	8	**60**	7
455	3	7	**64**
(b)			
640	**65**	7	6
543	5	**50**	6
455	1	4	**49**

Note: Bold values indicate efficiencies that should be as high as possible (ideally 100%). Non-bolded values indicate efficiencies that should be as low as possible.

Table 2 Simulated and experimentally measured transmission factors T for the color smiley APVE. The values are in percentages.

	640 nm (head)	543 nm (eyes)	455 nm (mouth)
T (sim)	83	82	87
T (exp)	84	82	66

The simulated (experimental) total efficiencies η_{tot} for the head, eyes, and mouth features are therefore 64% (55%), 49 (41%), and 56% (32%), respectively.

We further investigated the wavelength-dependent APVE properties using a fiber-coupled monochromator (Polychrome IV from TILL Photonics), whose output wavelength was tuned from 420 to 680 nm in steps of 10 nm. In contrast to the laser readouts where each beam had an individual, optimal waist value, the beam waist of the monochromator light at the APVE
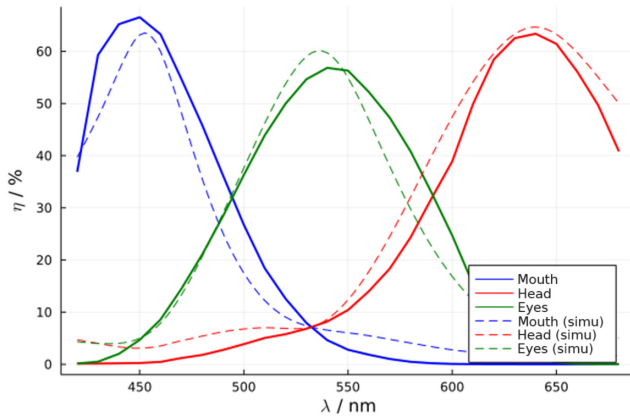

Fig. 4 Power conversion efficiencies of the multicolor APVE. The solid curves indicate the measured percentage of the output power transformed into the features mouth, eyes, and head, depending on the readout wavelength. The dashed lines correspond to simulated readouts.
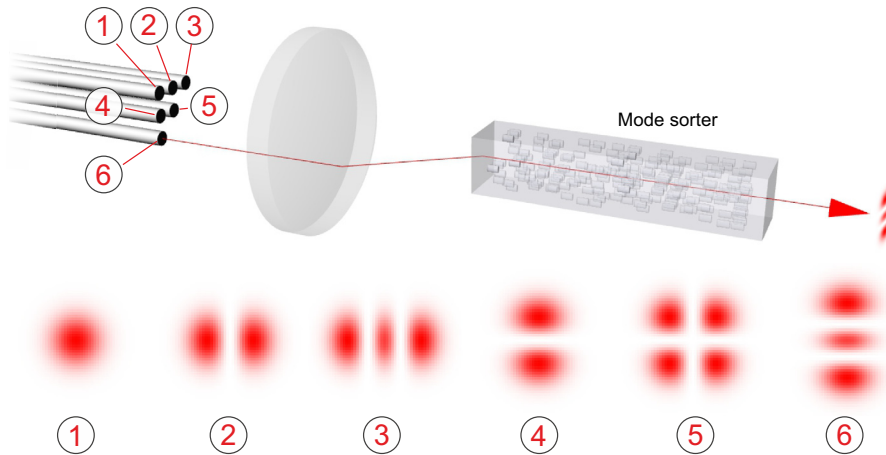
input facet was about 30 μm for all wavelengths (details are described in Sec. S2 of the Supplemental Material). While this means that the monochromator results are expected to be somewhat suboptimal, they nevertheless provide valuable information about the wavelength dependence of the APVE.

At each wavelength, we took images of the input beam and the APVE output (see data in Sec. S2 of the Supplemental Material), which allowed us to calculate wavelength-dependent power conversion efficiencies according to Eq. (1) for each spatial feature (mouth, eyes, and head). These efficiencies are plotted in Fig. 4. Of note, the peaks appear at wavelengths that almost exactly match the targets at 455, 543, and 640 nm. The measured efficiencies η at these wavelengths are 63%, 57%, and 63% and thus are close to the simulation values obtained from the laser readouts, as shown in Table 1(a). Interestingly, the blue monochromator image of the mouth shows a significantly higher efficiency than the respective experimental blue laser readout (63% versus 49%), which can presumably be ascribed to small differences in the readout beam profiles. Indeed, while the blue laser profile was slightly elliptic, the monochromator beam was almost perfectly Gaussian.

Figure 4 further contains data from the simulated readouts (dashed lines), which resemble the experimental data. To match the experimental conditions, these simulations assumed a beam waist of 30 μm for all readout wavelengths, which causes the peak efficiency values to be slightly lower than the values in Table 1, which assumes readouts taken at the designed waist values.

3.3 Angular Multiplexing

The high angular selectivity of a photonic volume element allows for encoding different outputs for varying input angles. This characteristic makes APVEs highly interesting for tasks such as mode-division multiplexing and sorting. To investigate the feasibility of angular multiplexing for our approach, we designed an APVE measuring only 0.1 mm × 0.1 mm × 4 mm and containing 55 × 14 × 400 voxels, which produces different HG modes, depending on the angle of incidence (AOI) of a Gaussian readout beam.

Such a device could be used as a mode-division multiplexer to enhance data transfer speed as sketched in Fig. 5: multiple

Fig. 5 Principle of mode-division multiplexing with our mode sorter. Multiple signals are delivered via single-mode fibers, arranged in a triangle. A lens gives each input beam a specific AOI. The APVE transforms each input beam into one of six different HG modes.
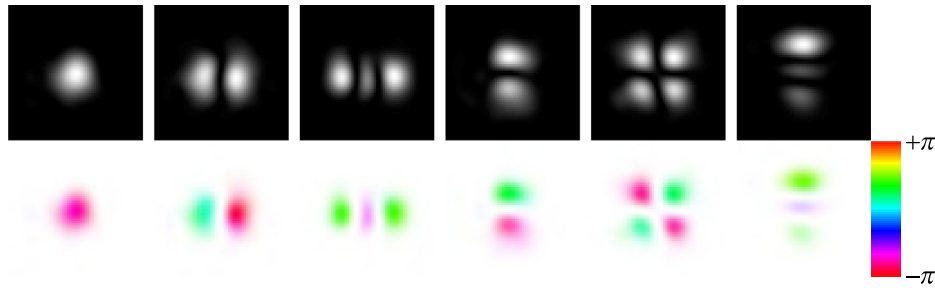
Fig. 6 Simulated results from the mode sorter. The images show intensities (top row) and phases when reading out the APVE with a Gaussian beam ($w_0 = 25$ μm, $\lambda_0 = 640$ nm) at six different AOIs. Each angle produces a different HG mode at the output. The saturation of the phase images is weighted by the intensity for enhanced clarity.
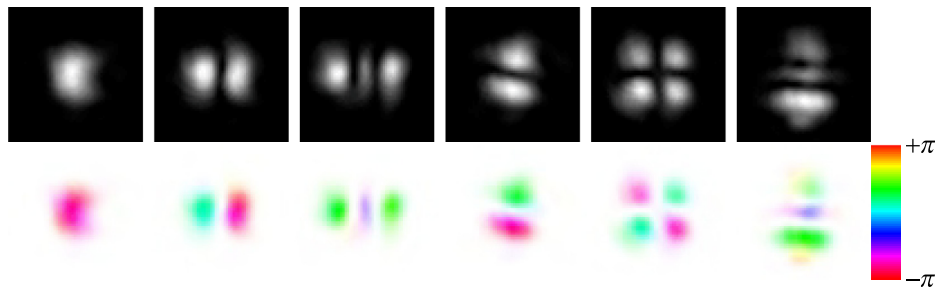

Fig. 7 Experimental results from the mode sorter. The images show intensities (top row) and phases when reading out the APVE with a Gaussian beam ($w_0 = 25$ μm, $\lambda_0 = 640$ nm) at six different incidence angles.

signals are delivered by single-mode fibers in a triangular arrangement, which has been shown to facilitate high HG mode-conversion efficiencies.[26] The fiber ends are in the focal plane of a convex lens, which collimates the light leaving the fiber outputs and sends it into the APVE at different fiber-specific propagation angles. The APVE converts each signal into a particular HG mode traveling in parallel to the optical axis, such that it can be efficiently coupled into a single multimode fiber.

We designed a mode-sorting APVE for readout with a Gaussian input of 640 nm wavelength and a 25 μm waist. Altering the input beam's AOI by merely 1.4 deg (defined in air) transforms the output field from one particular HG mode to another. In total, we encode six different HG modes, as shown in Fig. 5.

Figure 6 shows the output intensities and phases resulting from a simulated readout of the mode-sorting APVE. The matching experimental data are shown in Fig. 7. For both simulation and experiment, the numerical aperture (NA) at the output needs to be reduced to block stray light produced by the element. This reduces the overall light efficiency but enhances the spatial quality of the generated modes. In simulation, the NA was restricted to 0.02, in experiment to about 0.05.

As for the APVEs discussed previously, the overall quality of the mode sorter is governed by two factors: (i) the purity of the generated modes and (ii) the transmission of the APVE quantified by parameter T. Although the element itself absorbs almost no light, there is some power loss caused by the aperture stop restricting the imaging NA. We quantified point (i) by calculating efficiency values in analogy to Eq. (1) and taking the different HG modes as target fields,

$$\eta_{i,j} = \left| \int_A \mathrm{HG}_{i,j} u^*_{\mathrm{out}} \mathrm{d}A \right|^2, \tag{3}$$

where $\mathrm{HG}_{i,j}$ and u^*_{out} represent the target mode and conjugate output field with their total powers normalized to 1, respectively. An efficiency value of $\eta_{i,j} = 1$ means that the field has been shaped into a perfect $\mathrm{HG}_{i,j}$ mode, whereas $\eta_{i,j} = 0$ means that the field is orthogonal to this mode. Tables 3 and 4 contain efficiency values of the simulated and experimental mode sorter.

Table 3 Simulated efficiency values $\eta_{i,j}$ in percent. For each input angle, the numbers state the respective power fractions of the transmitted output light that is shaped into the corresponding HG modes.

Input angle no.	HG_{00}	HG_{10}	HG_{20}	HG_{01}	HG_{11}	HG_{02}
1	**90.6**	0.9	0.6	2.0	0.1	0.3
2	0.2	**89.1**	0.9	0.3	3.4	0.1
3	0.9	0.5	**90.2**	0.4	0.2	0.1
4	0.9	1.1	0.2	**87.2**	0.1	0.4
5	0.1	1.0	0.0	0.2	**93.9**	0.2
6	1.1	0.1	0.1	1.6	0.1	**79.6**

Note: Bold values indicate efficiencies that should be as high as possible (ideally 100%). Non-bolded values indicate efficiencies that should be as low as possible.

Table 4 Experimental efficiency values $\eta_{i,j}$ in percentages.

| Input angle no.	HG$_{00}$	HG$_{10}$	HG$_{20}$	HG$_{01}$	HG$_{11}$	HG$_{02}$
1	**88.4**	1.1	2.6	0.3	5.0	3.5
2	0.3	**87.0**	0.3	1.8	0.7	2.5
3	0.7	0.5	**83.8**	0.1	0.1	0.2
4	0.6	1.6	0.1	**83.7**	0.4	4.4
5	2.3	1.4	0.7	0.6	**86.6**	1.2
6	1.0	1.4	1.2	4.5	1.3	**65.7**

Note: Bold values indicate efficiencies that should be as high as possible (ideally 100%). Non-bolded values indicate efficiencies that should be as low as possible.

Table 5 Simulated and experimental transmission values T. For each mode, the numbers state the output/input power ratio in percentages.

	HG$_{00}$	HG$_{10}$	HG$_{20}$	HG$_{01}$	HG$_{11}$	HG$_{02}$
T (sim)	50.0	49.2	49.5	42.2	57.9	48.9
T (exp)	21.6	29.6	20.4	38.8	33.0	32.3

The off-diagonal terms represent undesired crosstalks into neighboring channels. The purest modes have efficiency values of 90% in the simulation and 88% in the experiment. The highest cross talk values are 3% for the simulation and 5% for the experiment.

The mode-dependent transmission of the APVE (ii), including both losses due to scattering and spatial filtering by the restricted imaging NA, are summarized in Table 5. Moreover, the dependence of the transmission and the maximum cross talk with respect to the restricted NA are shown in Fig. 8. This shows that the stray light that is not converted to the desired modes by the device has mostly high spatial frequencies, orthogonal to
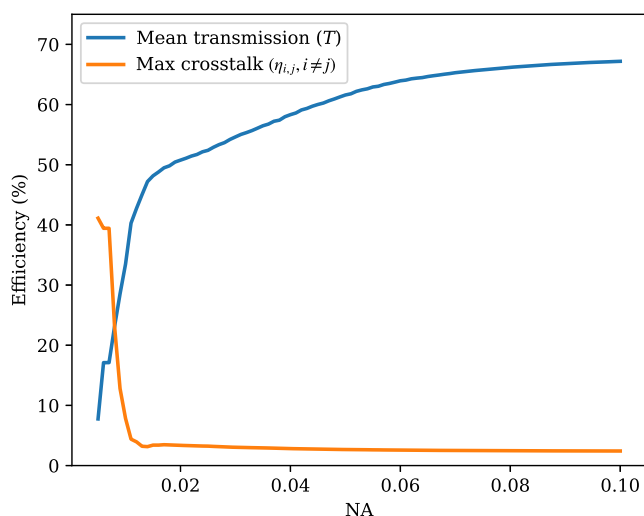
Fig. 8 Evolution of the transmission T and the maximum crosstalk in function of the restricted NA.

the desired modes, and that the quality of the mode conversion is very robust with respect to this unconverted light.

These results are still far from what could be theoretically obtained with a gradient index design,[27] but they are surprisingly good for a binary design. Introducing different types of voxels as new degrees of freedom for the inverse design optimization could significantly improve the capabilities of these mode multiplexers and approach the maximum performance of gradient index designs, for which a mature manufacturing technology is not yet available in glass.

4 Discussion

In this discussion section, we place our method in the context of related technological approaches.

4.1 Optically Recorded Volume Holograms

An important difference between traditional volume holograms and our APVEs exists in the physics of their creation. Traditional holograms are optically recorded by transferring the properties of interference patterns into a photosensitive material, such as a photopolymer[28,29] or a photorefractive crystal,[30] which naturally comes with limitations. First, each desired function must be physically realized at the recording step, which becomes unfeasible for advanced multiplexing applications. Second, one is bound to a limited number of suitable photosensitive materials. Finally, the dynamic range of optically recorded holograms is quickly consumed by only a few multiplexed recordings, which has an adverse effect on the obtainable diffraction efficiency.[10]

4.2 Metaholograms

In contrast to the APVE concept presented here, metaholograms rely on nanostructured metallic or dielectric surfaces, on which "meta-atoms" interact with light in predefined ways.[31–34] While the concept has proven to be especially powerful for wavelength and polarization-multiplexing tasks, angular multiplexing, i.e., the generation of different output fields at varying input angles, appears harder to achieve: only up to four multiplexed fields could be generated upon a large angular variation of more than 60 deg.[35] Some folded multiplane designs using metasurfaces have been realized recently to increase the multiplexing capabilities of these metaholograms.[36] Yet, the advantages of using metasurfaces in this context seems limited, since three reflections are required to achieve only a three-mode sorter, which is not significantly better than what more conventional cascaded diffractive optical elements can provide.[9]

4.3 Silicon Photonics

The field of silicon photonics,[37,38] i.e., the manufacturing and use of photonic integrated circuits inside silicon, has been attracting considerable attention for more than a decade. The fabrication of photonic chips can rely on existing infrastructure and lithographic techniques used in the electronic semiconductor industry and enables structure sizes down to a few nanometers. The field of silicon photonics is comparably mature, and the demonstration of wavelength multiplexing, for instance, dates back to the 1990s[39] and has been further developed toward high integration by employing modern tools of inverse design.[40] Spatial multimode operations were developed later, but are likewise possible in a highly integrated fashion.[41] Compared with silicon photonics, which is bound to infrared wavelengths,

our approach offers a wavelength window reaching down to the ultraviolet (UV), depending on the substrate, and is potentially applicable to a larger variety of materials offering different optical properties, including electro-optical and nonlinear ones. Furthermore, glasses as substrate facilitate novel applications linking optical and microfluidic technologies[42] and allow for easier light coupling compared with silicon, where mode mismatch can cause important insertion losses.[43] Lastly, the manufacturing of 3D devices is more innate to direct laser writing than it is to standard lithographic techniques[44] and also puts lower demands on the required infrastructure (no clean room required).

4.4 Writing Voxels for Data Storage

From the manufacturing point of view, our approach is related to storing data by writing of voxels inside polymers or glass.[45,46] This application has already reached an impressive maturity level, employing birefringent multilevel voxels.[47] However, in contrast to our application, data storage applications put significantly lower demands on the knowledge about the quantitative 3D properties of a single voxel, as well as their reproducible and spatially invariant fabrication, since they can be read out sequentially, and any slight deviation from the assumed voxel shape would be irrelevant, since only a few bits are encoded in a single voxel. Conversely, hundreds of thousands of voxels act jointly on the readout light in our APVEs, such that even small systematic errors at the single voxel level would have pronounced adverse effects on the sculpted fields.

5 Conclusion and Summary

We present a design and fabrication concept for robust and light efficient APVEs. Our design algorithm uses a mode-matching method and numerical beam propagation. The manufacturing is based on directly writing an optimized 3D arrangement of voxels into the volume of a transparent dielectric such as glass using a focused femtosecond laser. Each voxel consists of a small volume ($\sim 1.75~\mu m \times 7.5~\mu m \times 10~\mu m$) of slightly increased RI. Precise knowledge of the properties of a single voxel, in conjunction with an advanced fabrication technique, allowed us to physically realize APVEs of high efficiencies of up to 80%.

We experimentally realize three different APVE designs demonstrating different functionalities: an intensity shaper turning a Gaussian beam into a smiley-shaped light distribution, a wavelength multiplexer producing different parts of the smiley for three different readout wavelengths, and a spatial mode multiplexer, which converts a Gaussian input beam into particular HG modes, depending on the AOI.

While our proof-of-concept studies already show unprecedented performance, our APVE concept still has room for improvement in several respects and promises significantly higher efficiency and more complex functionalities in the future. For instance, our APVEs are made from a single voxel type, i.e., they are binary devices. However, it is straightforward to extend the design concept to nonbinary devices. On the manufacturing side, the use of varying laser powers, focus shapes, or multipass writing could be used to fabricate multiple different RI profiles. Nonbinary devices will be able to store more information and exhibit higher efficiencies. In addition, our concept is extensible to different types of substrates, including birefringent, electro-optic, and nonlinear substrates, potentially offering the possibility of polarization shaping, dynamic, or even erasable ferroelectric APVEs.[48]

Code, Data, and Materials Availability

Data underlying the results presented in this paper are not publicly available at this time but may be obtained from the authors upon reasonable request.

References

1. T. D. Rossing and C. J. Chiaverina, *Photonics—Light in the Twenty-First Century*, pp. 333–355, Springer International Publishing, Cham (2019).
2. H. Rubinsztein-Dunlop et al., "Roadmap on structured light," *J. Opt.* **19**(1), 013001 (2016).
3. A. Forbes, M. de Oliveira, and M. R. Dennis, "Structured light," *Nat. Photonics* **15**(4), 253–262 (2021).
4. M. Piccardo et al., "Roadmap on multimode light shaping," *J. Opt.* **24**(1), 013001 (2021).
5. D. J. Richardson, J. M. Fini, and L. E. Nelson, "Space-division multiplexing in optical fibres," *Nat. Photonics* **7**(5), 354–362 (2013).
6. G. Li et al., "Space-division multiplexing: the next frontier in optical communication," *Adv. Opt. Photonics* **6**(4), 413–487 (2014).
7. P. J. Winzer, D. T. Neilson, and A. R. Chraplyvy, "Fiber-optic transmission and networking: the previous 20 and the next 20 years," *Opt. Express* **26**(18), 24190–24239 (2018).
8. B. J. Puttnam, G. Rademacher, and R. S. Luís, "Space-division multiplexing for optical fiber communications," *Optica* **8**(9), 1186–1203 (2021).
9. N. U. Dinc et al., "Computer generated optical volume elements by additive manufacturing," *Nanophotonics* **9**(13), 4173–4181 (2020).
10. X. Porte et al., "Direct (3 + 1) d laser writing of graded-index optical elements," *Optica* **8**(10), 1281–1287 (2021).
11. J. Moughames et al., "Three-dimensional waveguide interconnects for scalable integration of photonic neural networks," *Optica* **7**(6), 640–646 (2020).
12. Y. Luo et al., "Computational imaging without a computer: seeing through random diffusers at the speed of light," *eLight* **2**(1), 1–16 (2022).
13. K. Liao et al., "All-optical computing based on convolutional neural networks," *Opto-Electron. Adv.* **4**(11), 200060 (2021).
14. P. Günter and J.-P. Huignard, *Photorefractive Materials and Their Applications*, Springer (2007).
15. H. J. Coufal, D. Psaltis, and G. T. Sincerbox, *Holographic Data Storage*, Springer (2000).
16. Y. Wakayama et al., "Mode demultiplexer using angularly multiplexed volume holograms," *Opt. Express* **21**(10), 12920–12933 (2013).
17. T. D. Gerke and R. Piestun, "Aperiodic volume optics," *Nat. Photonics* **4**(3), 188–193 (2010).
18. G. Douglass et al., "Two dimensional gradient-index beam shapers fabricated using ultrafast laser inscription," *Opt. Express* **30**, 40592–40598 (2022).
19. N. Barré et al., "Tomographic refractive index profiling of direct laser written waveguides," *Opt. Express* **29**(22), 35414–35425 (2021).
20. U. G. Būtaitė et al., "How to build the optical inverse of a multimode fibre," arXiv:2204.02865 (2022).

21. L. G. Wright et al., "Nonlinear multimode photonics: nonlinear optics with many degrees of freedom," *Optica* **9**, 824–841 (2022).
22. O. Lib and Y. Bromberg, "Quantum light in complex media and its applications," *Nat. Phys.* **18**(9), 986–993 (2022).
23. R. Berlich et al., "Fabrication of computer-generated holograms using femtosecond laser direct writing," *Opt. Lett.* **41**(8), 1752–1755 (2016).
24. M. Feit and J. Fleck, "Light propagation in graded-index optical fibers," *Appl. Opt.* **17**(24), 3990–3998 (1978).
25. A. Jesacher and M. J. Booth, "Parallel direct laser writing in three dimensions with spatially dependent aberration correction," *Opt. Express* **18**(20), 21090–21099 (2010).
26. N. K. Fontaine et al., "Laguerre–Gaussian mode sorter," *Nat. Commun.* **10**(1), 1–7 (2019).
27. N. Barré and A. Jesacher, "Inverse design of gradient-index volume multimode converters," *Opt. Express* **30**(7), 10573–10587 (2022).
28. W. Colburn and K. Haines, "Volume hologram formation in photopolymer materials," *Appl. Opt.* **10**(7), 1636–1641 (1971).
29. J. Jialing et al., "A review of photopolymers on holography volume data storage," *Opto-Electron. Eng.* **46**(3), 180552 (2019).
30. L. Hesselink et al., "Photorefractive materials for nonvolatile volume holographic data storage," *Science* **282**(5391), 1089–1094 (1998).
31. N. Yu and F. Capasso, "Flat optics with designer metasurfaces," *Nat. Mater.* **13**(2), 139–150 (2014).
32. B. Walther et al., "Spatial and spectral light shaping with metamaterials," *Adv. Mater.* **24**(47), 6300–6304 (2012).
33. J. Scheuer, "Metasurfaces-based holography and beam shaping: engineering the phase profile of light," *Nanophotonics* **6**(1), 137–152 (2017).
34. A. H. Dorrah and F. Capasso, "Tunable structured light with flat optics," *Science* **376**(6591), eabi6860 (2022).
35. J. Jang et al., "Independent multichannel wavefront modulation for angle multiplexed meta-holograms," *Adv. Opt. Mater.* **9**(17), 2100678 (2021).
36. J. Oh et al., "Adjoint-optimized metasurfaces for compact mode-division multiplexing," *ACS Photonics* **9**(3), 929–937 (2022).
37. B. Jalali and S. Fathpour, "Silicon photonics," *J. Lightwave Technol.* **24**(12), 4600–4615 (2006).
38. S. Y. Siew et al., "Review of silicon photonics technology and platform development," *J. Lightwave Technol.* **39**(13), 4374–4389 (2021).
39. P. Trinh et al., "Silicon-on-insulator (SOI) phased-array wavelength multi/demultiplexer with extremely low-polarization sensitivity," *IEEE Photonics Technol. Lett.* **9**(7), 940–942 (1997).
40. A. Y. Piggott et al., "Inverse design and demonstration of a compact and broadband on-chip wavelength demultiplexer," *Nat. Photonics* **9**(6), 374–377 (2015).
41. C. Li, D. Liu, and D. Dai, "Multimode silicon photonics," *Nanophotonics* **8**(2), 227–247 (2019).
42. P. Minzioni et al., "Roadmap for optofluidics," *J. Opt.* **19**(9), 093003 (2017).
43. L. Carroll et al., "Photonic packaging: transforming silicon photonic integrated circuits into photonic devices," *Appl. Sci.* **6**(12), 426 (2016).
44. S. J. B. Yoo, B. Guan, and R. P. Scott, "Heterogeneous 2D/3D photonic integrated microsystems," *Microsyst. Nanoeng.* **2**, 16030 (2016).
45. J. H. Strickler and W. W. Webb, "Three-dimensional optical data storage in refractive media by two-photon point excitation," *Opt. Lett.* **16**(22), 1780–1782 (1991).
46. E. Glezer et al., "Three-dimensional optical storage inside transparent materials: errata," *Opt. Lett.* **22**(6), 422–422 (1997).
47. J. Zhang et al., "Seemingly unlimited lifetime data storage in nanostructured glass," *Phys. Rev. Lett.* **112**(3), 033901 (2014).
48. X. Xu et al., "Femtosecond laser writing of lithium niobate ferroelectric nanodomains," *Nature* **609**, 496–501 (2022).
49. G. Della Valle, R. Osellame, and P. Laporta, "Micromachining of photonic devices by femtosecond laser pulses," *J. Opt. A: Pure Appl. Opt.* **11**(1), 013001 (2008).
50. N. Bisch et al., "Adaptive optics aberration correction for deep direct laser written waveguides in the heating regime," *Appl. Phys. A* **125**, 364 (2019).
51. J. R. Fienup, "Phase-retrieval algorithms for a complicated optical system," *Appl. Opt.* **32**(10), 1737–1746 (1993).

Biographies of the authors are not available.